ARTICLE

Bioactive Core–Shell CaF₂ Upconversion Nanostructure for Promotion and Visualization of Engineered Bone Reconstruction

Zhihao Li,[§] Haoran Liu,[§] Rui Wang,[§] Chenhui Ji, Yan Wei, Miusi Shi, Yingqian Wang, Yaping Du, Yufeng Zhang,* Quan Yuan,* and Chunhua Yan

Read Online

ACCESS | Metrics & More | Article Recommendations | Supporting Information

ABSTRACT: Inorganic ion metabolism plays significant roles in various life processes including signal transduction, substance exchange, and cellular constructions. Regulation and monitoring of ion metabolism offer great promise to modulate biological activities and provide insights into related mechanisms. Here, a synergistic nanodepot based on a bioactive core−shell CaF₂ upconversion nanostructure that integrates multiple mineral ions for metabolic regulation was built for the acceleration and monitoring of the biomineralization process. Multiple mineral ions released from the nanodepots can accelerate the growth of inorganic crystals and enhance the production of organic matrixes, synergistically facilitating the regeneration of bone defects *in vivo*. During the process, such a nanodepot can be constructed to specifically recognize osteoblasts for the monitoring of biomineralization. This nanoprobe represents an efficient strategy to promote and monitor biomineralization-related metabolic activities with applications in fundamental research, disease diagnosis, and regenerative medicine.

KEYWORDS: *biomineralization, upconversion, bioactive glasses, fluoride, tissue engineering*
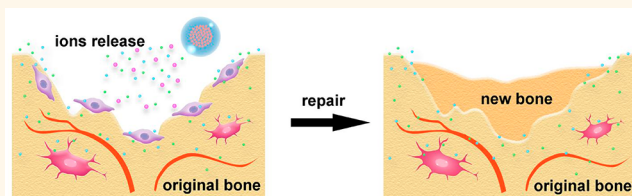
Metabolic regulation is the most essential requirement for cellular functions and survival.[1,2] It covers a host of biochemical reactions to generate energy and to provide precursor molecules to elaborate life processes.[3−5] Most of these metabolic reactions are tightly involved with inorganic ions, which usually trigger a series of biological activities through interacting with enzymes,[6,7] proteins,[8,9] and nucleic acids.[10] For instance, inorganic ions can serve as activators to stimulate the activity of biomolecules, playing important roles in signal transduction, biological synthesis, and substance exchanges.[11−13] Moreover, ions can also be directly chelated with biomolecules to form inorganic−organic hybrid complexes for macrostructure formation and cell construction.[14,15] In this condition, different kinds of inorganic ions deposit onto the organic matrixes to produce mineral crystals, further assembling to hierarchically sophisticated structures.[16,17] Such mineralized structures usually exhibit exquisite biomechanical properties and extraordinary functions including locomotion, protection, support, and mineral storage, constituting an indispensable part of living organisms.[18−20] During this biologically mediated mineralization process, the species

and concentrations of mineral ions are in dynamic equilibrium to maintain local homeostasis.[21] As a result, the morphology, orientation, and biogeochemical composition of crystals can be precisely controlled with delicate modulation of their biomechanical properties and functions.[17,22] Once the metabolic homeostasis of mineral ions is out of control, the structure and function of biomineralized crystals could be severely affected, leading to the deficiency of tissues and further occurrence of diseases such as disability,[23,24] tumor,[25] and even death.[26] In this regard, regulation and monitoring of mineral ion metabolism can not only offer insight into related physiological and pathological biomineralization mechanisms but also hold great promise for the development of efficient
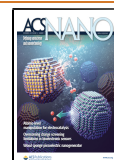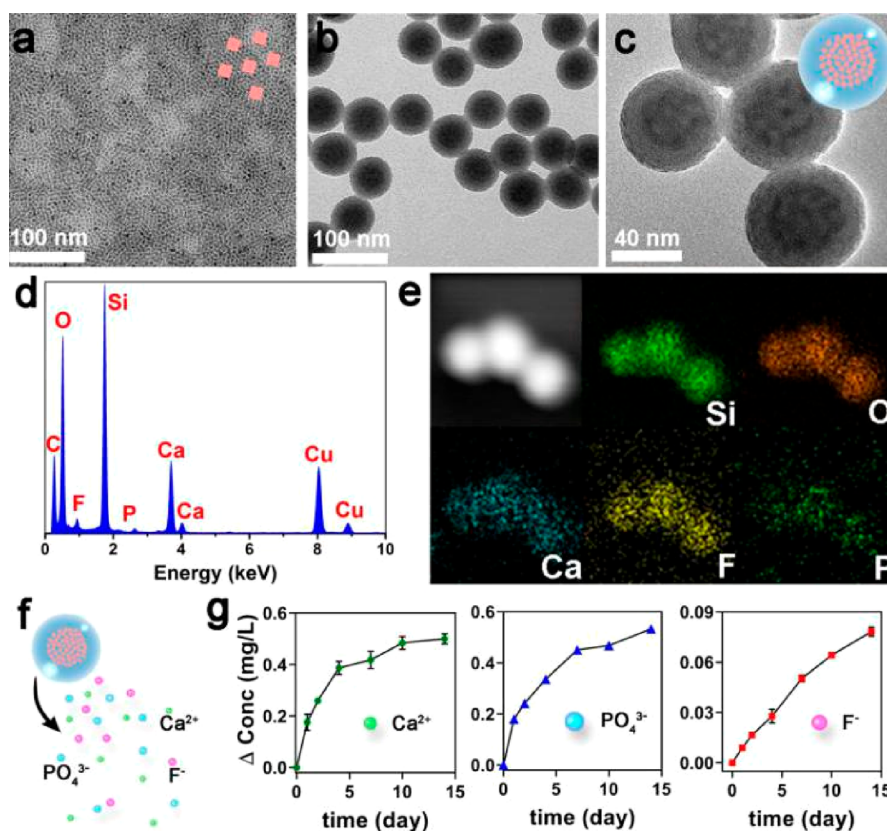
Figure 1. (a) TEM image of CaF$_2$ nanoparticles. (b and c) TEM images of CaF$_2$@BGs-integrated mineral nanodepots. (d) Energy dispersive spectrum (EDS) analysis and (e) corresponding elemental mappings of integrated mineral nanodepots. (f) Scheme for the release of mineral ions from nanodepots. (g) Concentration changes of mineral ions released from mineral nanodepots.

treatment for biomineralization-related bone defects, cancer, and metabolic diseases.

In this work, a core–shell CaF$_2$ upconversion nanostructured mineral nanodepot that integrates the functions of homeostasis regulation and imaging was constructed for the regulation and monitoring of biomineralization-related ion metabolism. To be specific, this nanodepot introduces multiple mineral ion species and improves the local homeostasis by accelerating the nucleation and growth of mineral crystals. Moreover, the nanodepot also stimulates the proliferation and differentiation of osteoblasts, enhancing the expression of organic matrixes for assembly with inorganic crystals. Both accelerated crystal growth and enhanced organic matrixes synergistically facilitate the biomineralization. Further *in vivo* studies demonstrated the excellent biocompatibility of the nanodepot, as well as a robust capacity for the regeneration of bone tissues. In the process of bone biomineralization, this nanoprobe integrated with target molecules can specifically recognize osteoblasts for the noninvasive, real-time, and *in situ* monitoring of biomineralization metabolism. Such an integrated mineral nanodepot represents a vivid example of the regulation and monitoring for biomineralization metabolism, offering insights into both biomineralization-related and metabolism-related physiological mechanisms with applications in disease prevention, tissue engineering, and regenerative medicine.

RESULTS AND DISCUSSION

Design and Preparation of the Integrated Mineral Nanodepots. In the biomineralization reactions of mammals,

inorganic mineral elements including calcium and phosphorus are significantly essential for metabolic regulation.[27,28] The ion forms of these two elements, Ca^{2+} and PO$_4^{3-}$, finally form hydroxyapatite under the control of osteoblasts, constituting the main inorganic components of bone.[29,30] Apart from calcium and phosphorus, as an important trace element, fluoride can accelerate the formation of inorganic crystals and increase the density of bone to enhance biomechanical properties.[31,32] In this regard, a platform containing calcium, phosphate, and fluoride has great potential for the promotion of bone-related biomineralization. Bioactive glasses (BGs), a kind of well-known material containing calcium, phosphorus, and silicon, have been regarded as effective candidates for bone regeneration owing to their robust osteoconductivity and biocompatibility.[33,34] CaF$_2$, a fluoride-rich and component-friendly matrix of upconversion nanomaterial, has found wide applications in bioimaging and therapy owing to its excellent biocompatibility.[35−38] In view of this, it can be estimated that the construction of an integrated mineral nanodepot combining BGs with CaF$_2$ would provide a highly promising strategy for the promotion and monitoring of biomineralization.

The synthesis of CaF$_2$@BGs integrated mineral nanodepots was based on a three-step method. At the onset, CaF$_2$ nanoparticles capped with oleic acids were synthesized *via* a previously reported method.[36] Transmission electron microscope (TEM) images (Figure 1a and Figure S1) show that CaF$_2$ nanoparticles appear as a monodisperse nanocube shape with a uniform size of about 5 nm. For the further integration of BGs, CaF$_2$ was then functionalized with bovine serum

albumin (BSA) to be water-soluble,[39] and then, a modified emulsion method was adopted to form a BG shell on the core CaF$_2$ nanoparticles.[40] As shown in Figure 1b, Figure 1c, and Figure S2, the CaF$_2$@BGs integrated mineral nanodepots present a core–shell structure with a core size of 40 nm and shell thinness of 10 nm. Besides, elemental analysis and mapping (Figure 1d and e) also indicate that the nanodepots contain multiple elements including Ca, F, P, Si, and O. XRD patterns in Figure S3 indicate that the peaks of CaF$_2$ and nanodepots match well with each other and are consistent with cubic crystal structure data of standard CaF$_2$ (JCPDS No. 01-087-0976). FTIR spectrum in Figure S4 presents a peak at 968 and 715 cm^{-1}, corresponding to the P–O–P bond and Ca–O–P bond in nanodepots. All these results suggest that integrated nanodepots with multicomponent minerals have been successfully synthesized. To investigate the capability of nanodepots for providing mineral ions, the integrated mineral nanodepots were dispersed into the aqueous solution and the release of mineral ions was monitored (Figure 1f). As shown in Figure 1g, there are increased levels of Ca^{2+}, PO$_4^{3-}$, and F$^-$ in the solution with the time increasing, indicating that such an integrated mineral nanodepot can offer additional F$^-$ for the metabolic regulation.
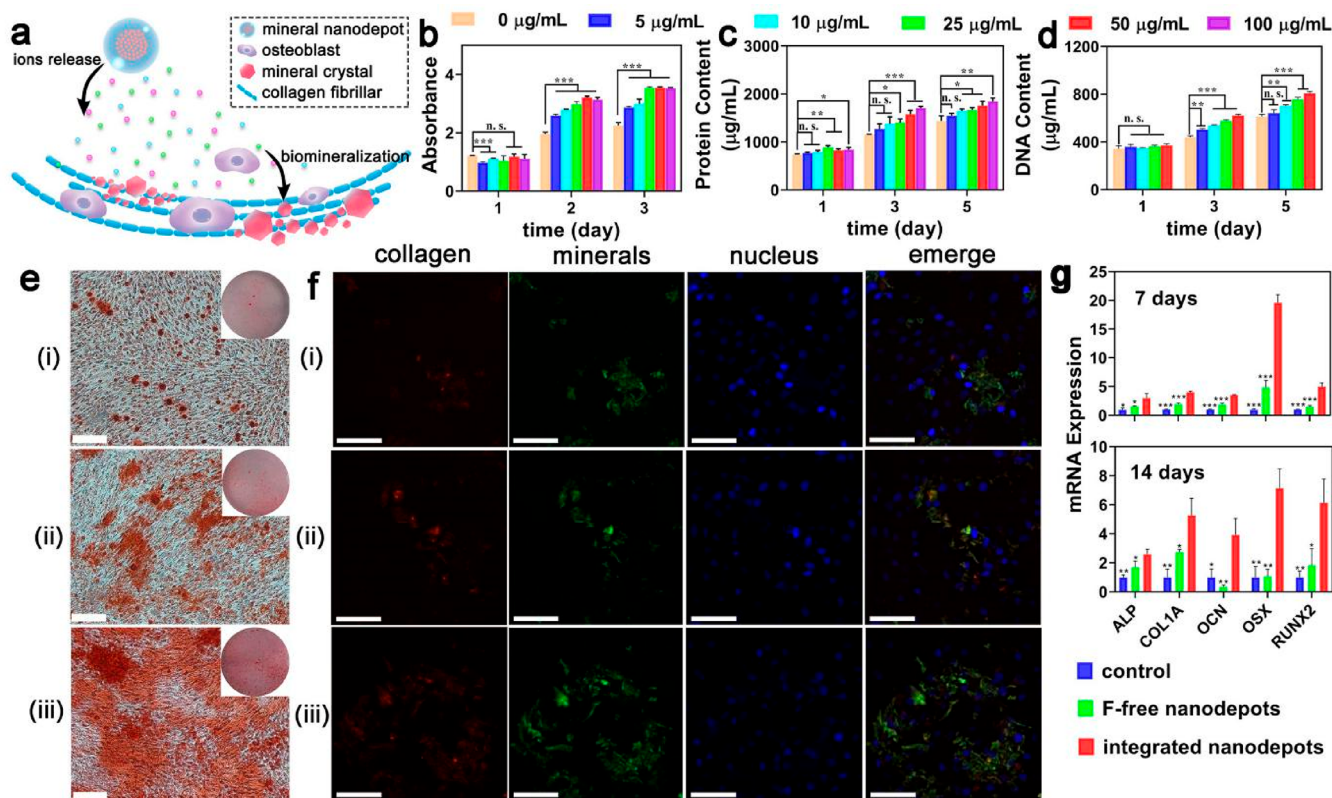
CaF$_2$@BGs Integrated Mineral Nanodepot-Promoted Mineralization of Fibrillar Collagens. To investigate the nanodepots' effect on mineralization, nanodepots were cultured with fibrillar collagens to observe the formation of crystals. A schematic of the formation of crystals is illustrated in Figure 2a. Specifically, nanodepots serve as the mineral source, and mineral ions released from the depots are deposited onto the surface of fibrillar collagens to form crystals. First, collagens were assembled with a uniform shape of fibers (Figure S5). To investigate the *in vitro* degradation of nanodepots, the CaF$_2$@BGs nanodepots were immersed into improved simulated body fluid (SBF), and TEM was performed to observe the morphology change of nanodepots at different reaction times (Figure S6). These TEM images indicate that the nanodepots can be gradually degraded to release mineral ions. Then, TEM was performed to characterize the formation of crystals with collagens. As shown in Figure 2b and c, both the system containing no depots and the system containing F-free nanodepots exhibit no obvious crystal formation. In contrast, it can be observed from Figure 2d and Figure S7 that the system containing CaF$_2$@BGs-integrated mineral nanodepots presents a large number of crystals on the surface of fibrillar collagens. A high-resolution TEM image shows that the crystals exhibit well-defined crystalline fringes in the system containing integrated mineral nanodepots (Figure 2e), suggesting that fluoride ions play a crucial role in the formation of mineral crystals. The interplanar distance of the mineral crystals is 0.35 and 0.28 nm, respectively, corresponding to the (002) facet and (211) facet of hydroxyapatite crystals. Besides, with the time increasing, the mineral crystals grow into large nanostructures (Figure S8). It has been reported that the introduction of F$^-$ can lower the solubility product (K_{sp}) of calcium phosphate.[41] According to the classical nucleation theory, a decrease in K_{sp} would contribute to a decrease in the supersaturation of the solution, consequently contributing to the improved rate of nucleation and growth of mineral crystals.[42,43] It means that within the same time a larger number of crystal nuclei would form in the solution containing F$^-$ than that in the solution without F$^-$. Such analysis based on classical nucleation theory
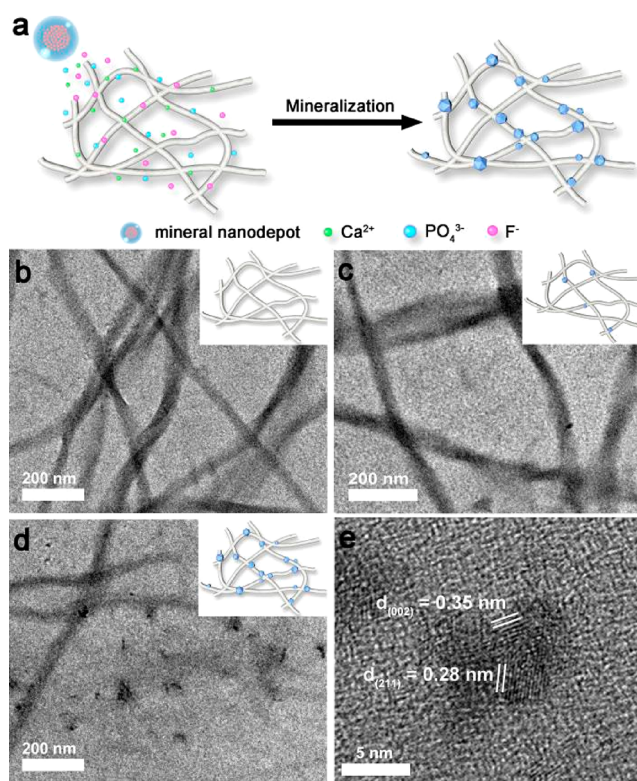
Figure 2. (a) Schematic illustration for the mineralization of fibrillar collagens based on nanoparticles. (b–d) TEM images of fibrillar collagens mineralized with (b) blank, (c) F-free nanodepots, and (d) integrated mineral nanodepots. (e) High-resolution TEM image of crystals on the surface of fibrillar collagens mineralized with integrated mineral nanodepots.

is consistent with the results of the aforementioned TEM characterizations, suggesting that multiple mineral ion-integrated nanodepots exhibit excellent capability for the promotion of crystal nucleation. The above assays thus clearly demonstrate the great promise of the CaF$_2$@BGs nanodepots in accelerating biomineralization.

CaF$_2$@BGs-Integrated Mineral Nanodepot-Promoted Calcium Mineralization of Osteoblasts. The integrated mineral nanodepots were further cultured with osteoblasts for mineralization promotion. As illustrated in Figure 3a, fibrillar collagens are produced by the osteoblasts, and at the same time, mineral ions released from the nanodepots are deposited onto the surface of collagen to form mineral crystals. First, nanodepots' effects on the variability of osteoblasts were tested as shown in Figure 3b. Besides, osteoblasts treated with CaF$_2$@BGs exhibit a higher level of cellular proteins and DNA than PBS (Figure 3c and d), indicating that the nanodepots exhibit excellent biocompatibility and good capability for promoting the proliferation of the osteoblasts. The distribution of nanodepots around osteoblasts observed by TEM and confocal microscopy indicates that more nanodepots are internalized by osteoblasts with the time increasing (Figures S9 and S10). Then, the calcium mineralization performance of integrated mineral nanodepots was investigated by Alizarin Red S staining, considering that Alizarin Red S can serve as an efficient indicator for the formation of crystals. As presented in Figure 3e, osteoblasts treated with integrated mineral nanodepots exhibit a much larger size of staining spots than those treated with only PBS and only F-free nanodepots.
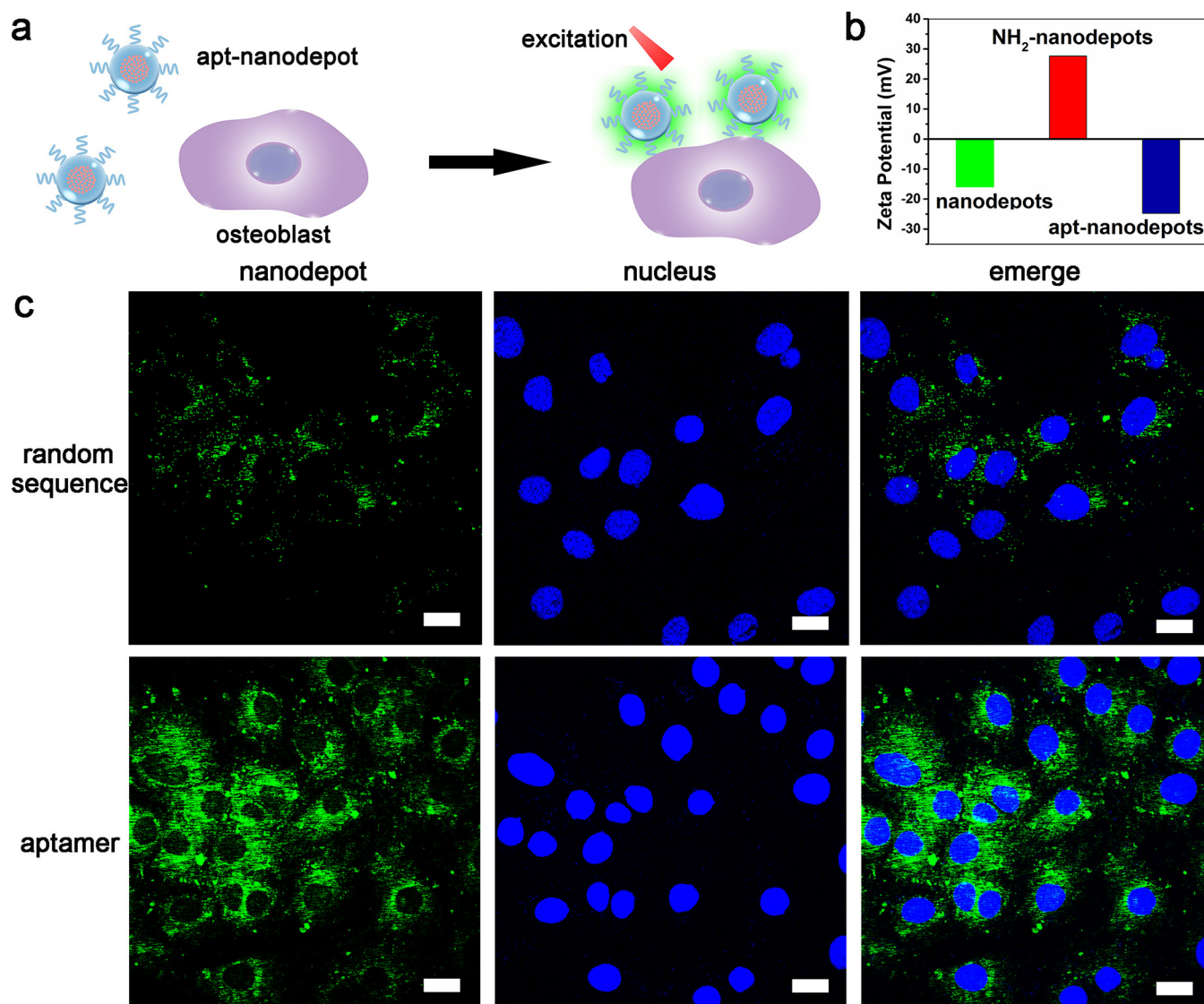
Figure 3. (a) Schematic illustration for the biomineralization of osteoblasts based on integrated mineral nanodepots. (b) Variability, (c) total cellular protein contents, and (d) total DNA contents of osteoblasts treated with CaF$_2$@BGs-integrated mineral nanodepots of different concentrations. (e) Photographs of Alizarin Red S staining in the culture of osteoblasts treated with only (i) PBS, (ii) F-free nanodepots, and (iii) CaF$_2$@BGs-integrated mineral nanodepots. (f) Confocal fluorescence microscopy images of the osteoblasts treated with only (i) PBS, (ii) F-free nanodepots, and (iii) CaF$_2$@BGs-integrated mineral nanodepots. Red, collagen fibers; blue, nucleus; green, mineral crystals. Scale bar: 200 μm. (g) qPCR analysis of bone markers of osteoblasts at day 7 and day 14. Data are presented with mean $\pm$ SD (n = 3), *P < 0.05, **P < 0.01, ***P < 0.001 (unpaired two-tailed Student's t-test).

Corresponding quantitative analysis in Figure S11 also presents a similar result. Additionally, confocal fluorescent microscopy was utilized to study the mineralization content at the cellular level. To visualize the mineralization landmarks, mineral crystals were labeled with tetracycline and fibrillar collagens were marked with DyLight-antibody. As shown in Figure 3f and Figure S12, integrated mineral nanodepots display a positive effect on the production of fibrillar collagens, mainly ascribed to the improved proliferation of osteoblasts. Besides, compared to the osteoblasts treated with only PBS and F-free nanodepots, osteoblasts treated with integrated mineral nanodepots generate much more mineral crystals, exhibiting robust capability for calcium mineralization. Furthermore, given that enhanced alkaline phosphatase (ALP) concentration has been regarded as a landmark for osteogenesis biomineralization,[21,44] the expression levels of ALP in osteoblasts were measured by a colorimetric assay. As shown in Figure S13, it is obvious that integrated mineral nanodepots can enhance the expression of ALP. A similar result was obtained for the quantification analysis of the ALP activity in these groups (Figure S14). qPCR was also performed to investigate the nanodepot-improved mineralization of cells. As shown in Figure 3g, osteoblasts treated with CaF$_2$@BGs-integrated mineral nanodepots exhibit higher levels of bone marker mRNA, indicating that CaF$_2$@BGs can promote the mineralization of osteoblasts. Taken together, all the results demonstrate that integrated mineral nanodepots can accelerate

the formation of mineral crystals and enhance the production of fibrillar collagens, synergistically promoting the calcium mineralization of osteoblasts.

Imaging of Osteoblasts Based on apt-CaF$_2$@BGs Nanodepots. Apart from the promotion of biomineralization, monitoring of the biomineralization process is also of significant importance to investigate relevant biological activities. A host of studies have reported that osteoblasts play a key role in bone formation, growth, and metabolism during the biomineralization progress.[45] Specifically, osteoblasts can synthesize and secrete specialized proteins and cross-linked collagen, composing the organic basis of biominerals.[46] Other necessary biological factors for bone biomineralization such as genes, enzymes, and matrix vesicles are also originated from osteoblasts.[47] Thus, osteoblasts could be utilized as model cells for the research of biomineralization, and imaging of osteoblasts may provide an efficient strategy to uncover biomineralization-related mechanisms. To endow the nanodepots with imaging capability, lanthanide ions, Er^{3+} and Yb^{3+}, were doped into the CaF$_2$ core to synthesize upconversion CaF$_2$:Yb,Er@BGs nanodepots.[35−37] Characterizations of CaF$_2$:Yb,Er and upconversion CaF$_2$:Yb,Er@BGs are presented in Figures S15−S18. Furthermore, to endow upconversion nanodepots with targeting ability, an aptamer, a nucleic acid sequence that can specifically recognize osteoblasts,[21,24] was functionalized onto the surface of aminopropyltriethoxysilane (APTES)-functionalized CaF$_2$:Yb,Er@BGs nanodepots (NH$_2$-

Figure 4. (a) Schematic illustration for the imaging of osteoblasts based on apt-nanodepots. (b) Zeta potential results of nanodepots, NH₂-nanodepots, and apt-nanodepots. (c) Confocal fluorescence microscopy images of the osteoblasts treated with random DNA-functionalized nanodepots and aptamer-functionalized nanodepots. Scale bar: 20 μm.

nanodepots) to construct imaging probes, apt-nanodepots (Figure S19). The scheme for osteoblast imaging with apt-nanodepots is illustrated in Figure 4a. Zeta potential results (Figure 4b) demonstrate that nanocomposites were negatively charged after the functionalization of the aptamer, indicating the successful construction of imaging probes. Confocal microscopy and flow cytometry were utilized to verify the binding of nanoprobes with osteoblasts. As presented in Figure 4c, strong upconversion luminescence signals were observed around the osteoblasts after treatment with apt-nanodepots. In contrast, when osteoblasts were treated with random sequence functionalized nanodepots (rDNA-nanodepots), almost no emission signal was observed, suggesting that rDNA-nano-depots possess an extremely weak binding affinity to osteoblasts. The binding ability of the aptamer and apt-nanodepots was also evidenced by flow cytometry analysis. Since the flow cytometry is not equipped with a 980 nm laser as a light source, the aptamer was labeled with FITC to provide fluorescence signals. Compared to the osteoblasts without treatment and osteoblasts treated with rDNA-nanodepots,

those treated with apt-nanodepots display an obvious peak shift with enhanced luminescence signal, further suggesting the robust interaction between apt-nanodepots and osteoblasts (Figure S20). All the results demonstrate that apt-nanodepots were successfully built for the imaging of osteoblasts.

CaF₂@BGs-Integrated Mineral Nanodepot-Promoted Biomineralization *in Vivo*. To investigate the biomineraliza-tion-promoting effect of integrated mineral nanodepots *in vivo*, rats with a subchondral bone defect were used as the standard model. Given that biomaterials must meet the requirement of biocompatibility for their use *in vivo*, the biocompatibility of integrated mineral nanodepots *in vivo* was evaluated by body weight monitoring, blood biochemistry, hematology examina-tion, and histological analysis. Over 30 days after implanting of materials into the model rats, the bodyweight of rats treated with integrated mineral nanodepots and F-free nanodepots all kept similar changes to the control group, respectively (Figure S21). This result served as an indicator that integrated mineral nanodepot and F-free nanodepot implantation does not cause systemic toxicity or affect the digestive systems and nutrient
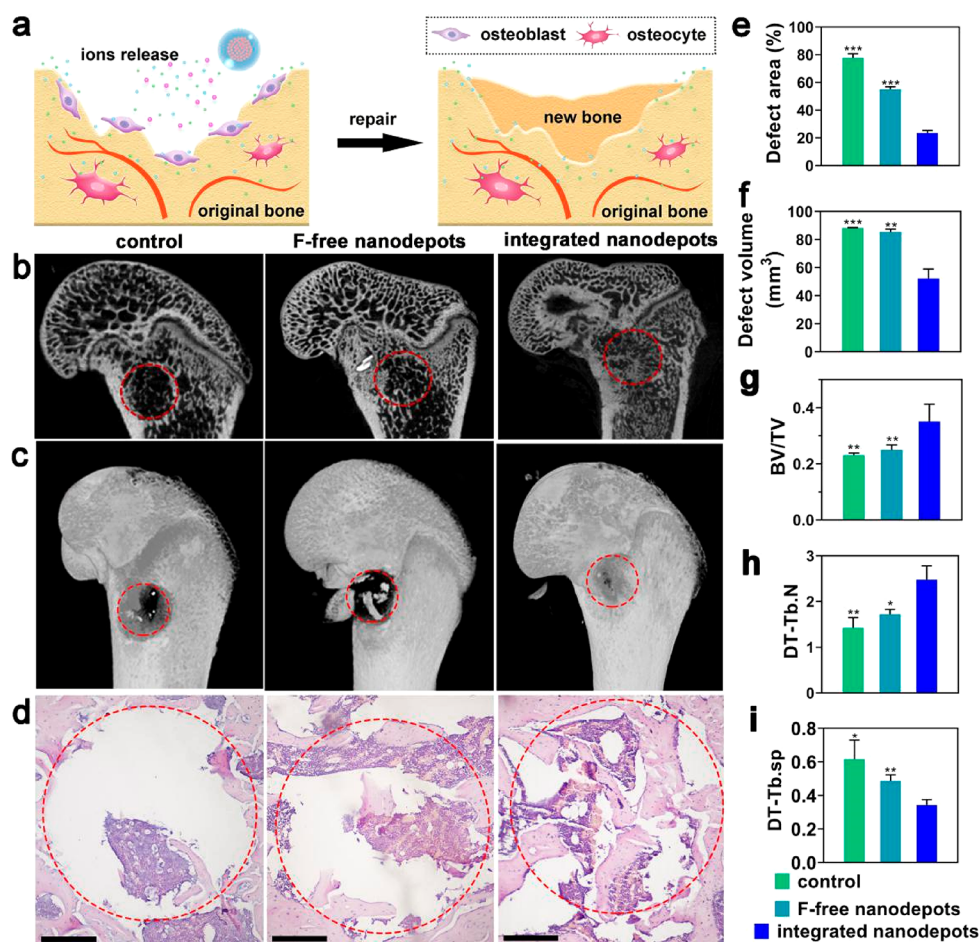
Figure 5. (a) Schematic illustration of biomineralization promotion based on CaF$_2$@BGs nanocomposites. (b) μ-CT reconstruction and (c) 3D isosurface rendering of the bone defect without treatment and treated with F-free nanodepots and integrated nanodepots. Red circles with dashed lines refer to the defect area. (d) Histomorphology analysis and (e) corresponding quantitative analysis of the tissues with only PBS, F-free nanodepots, and integrated nanodepots. Scale bar: 1 mm. Quantification of (f) defect volume, (g) bone volume density (BV/TV), (h) trabecular number (Tb. N), and (i) trabecular separation (Tb. sp) in the defect area. Data are presented as mean $\pm$ SD ($n = 3$), *P < 0.05, **P < 0.01, ***P < 0.001 (unpaired two-tailed Student's t-test).

transport. Microcomputed tomography (μ-CT) reconstruction results show that no nanodepots remain after 28 days, indicating that the nanodepots are highly degradable *in vivo* (Figure S22). Histological evaluations of several organs, including heart, liver, kidney, lung, and spleen (Figure S23), and blood biochemistry (Figure S24) do not show obvious morphology changes between all the materials-treated groups and the control group, indicating that both the integrated mineral nanodepots and F-free nanodepots have no obvious adverse effects on the tissues. These results thus preliminarily suggest that integrated mineral nanodepots are of good biocompatibility for *in vivo* biological applications.

The schematic illustration of biomineralization promotion based on integrated mineral nanodepots is presented in Figure 5a. After filling of nanodepots into the damaged area, μ-CT reconstruction and hematoxylin and eosin (H&E) staining were utilized to investigate the bone regeneration to access the bone repair effects of nanodepots. As shown in Figure 5b and c, when the rat is treated with integrated mineral nanodepots, the bone defect is almost completely repaired with the formation of substantial amounts of new bone. Contrastively, for the rats without treatment and the rats treated with F-free nanodepots, there is less new bone formation in the damaged area than those of rats treated with integrated mineral

nanodepots. Furthermore, H&E staining analysis (Figure 5d and e) presents that a large amount of newly formed bone was generated in the defect area of integrated mineral nanodepot-filled rats with enhanced expression of osteoblasts, whereas for the rats treated with only PBS and F-free nanodepots, lesser amounts of newly produced bone were regenerated in the damaged area. Certain microarchitectural parameters were also analyzed to evaluate the new bone formation. To be specific, bone volume/tissue volume (BV/TV) has been widely recognized as an indicator to reveal the amount of newly formed bone in the defect area. The trabecular number (Tb. N) is an important indicator of the density of new bone. In addition, trabecular separation (Tb. Sp) represents the space between trabecular bone and is another important indicator for bone density. Usually, a lower value of Tb. Sp reveals a higher density of new bone. As presented in Figure 5f and g, defect volume and BV/TV analysis indicate that the rats treated with integrated mineral nanodepots exhibited the lowest defect volume and the highest value of BV/TV with a maximum amount of newly formed trabecular bone in the defect area. The Tb. N analysis in Figure 5h shows that the integrated mineral nanodepot group also exhibits the highest bone density, indicating that integrated mineral nanodepots displayed excellent performance in bone regeneration. Similar
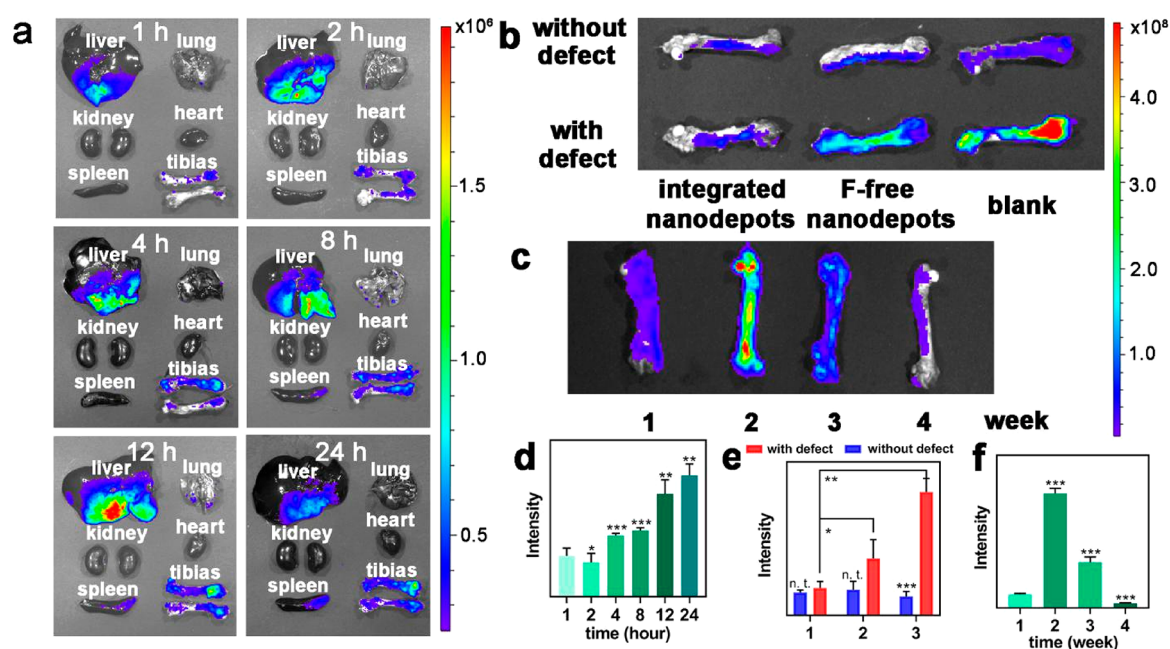
Figure 6. (a) Distribution of apt-nanodepots in the main organs and bone at different times. The rats used were without bone defect. (b) Imaging of osteoblasts in the bone without defect and in the bone defect of rats with only PBS, F-free nanodepots, and integrated nanodepots. The apt-nanodepots were injected at day 28, and tibias were collected 8 h after injection. (c) Imaging of osteoblasts in the bone defect of rats treated with integrated nanodepots for different times. Tibias were collected 8 h after injection of apt-nanodepots. (d−f) Quantitative analysis of (a)−(c), respectively. (e) (1) Integrated nanodepots, (2) F-free nanodepots; (3) control. Data are presented as mean ± SD (n = 3), *P < 0.05, **P < 0.01, ***P < 0.001 (unpaired two-tailed Student's t-test).

results were also obtained in the Tb. Sp analysis in Figure 5i. The Tb. Sp of the integrated mineral nanodepot group is the lowest, demonstrating the most intensive trabecular bone in the defect area. These findings demonstrate that integrated mineral nanodepots display outstanding capability in bone biomineralization.

Visualization of Bone Biomineralization Based on apt-CaF$_2$:Yb,Er@BGs Nanodepots. During the process of bone biomineralization, the expression of osteoblasts was imaged for the monitoring of bone biomineralization. Apt-nanodepots were intravenously injected for the specific imaging of osteoblasts. The targeting performance of apt-nanodepot probes was investigated by monitoring their *in vivo* distribution. As shown in Figure 6a and d, large amounts of nanoprobes reached the defected bone area with a much higher signal than other tissues, indicating that apt-nanodepots can selectively recognize the osteoblasts in bone areas. It is noted that liver and spleen exhibit the signals of nanodepots. This is mainly because liver and spleen are two major organs for the metabolism of nanomaterials, and as a result, nanodepots administered were sequestered and enriched in the liver and spleen.[48] Furthermore, apt-nanodepot nanoprobes were exploited to investigate the expression of osteoblasts in rats treated with only PBS, only F-free nanodepots, and integrated mineral nanodepots for 4 weeks, respectively. As presented in Figure 6b and e, compared with the rats treated with only PBS and only F-free nanodepots, rats treated with integrated mineral nanodepots exhibited the lowest signal intensity. According to previous reports,[49,50] for the injured bones, mesenchymal cells would be recruited to the injured tissues and differentiate to osteoblasts. Thus, the expression level of osteoblasts would be enhanced to accelerate the biomineralization-related bone repair process. For the repaired bones that return to the normalized condition, the

expression level of osteoblasts would be lower than that in injured bones, contributing to the lower signals of integrated nanodepot-treated defect bones than control groups. Besides, it is noted that the signals of nanodepots were observed at the tissue level, rather than at the injury area. There are two possible reasons. First, osteoblasts exist in the whole bone tissues, so the signal of osteoblasts is distributed in the whole tissue. Second, the previous literature[21] indicates that the aptamer used may bind with marrow mesenchymal cells and osteoblast precursors, and these two kinds of cells distribute at the tissue level. These results indicate that apt-nanodepots can be used as an efficient tool for monitoring osteoblasts expression, holding great promise for the investigation of biomineralization mechanisms. Moreover, among the group with defects, the integrated nanodepot-treated group exhibits the lowest expression of osteoblasts, approaching the state of the group without defect. The result indicates that the integrated nanodepot-treated group exhibits the state similar to normal rats with physiological homeostasis in the bone repaired area, suggesting the excellent regeneration performance of integrated nanodepots. Figure 6c and f present the expression of osteoblasts in rats treated with integrated nanodepots for different times. The results show that 2 weeks after treatment, the level of osteoblasts in the defect area reaches a peak value. During the third week and the fourth week, the expression of osteoblasts gradually decreases, approaching the state similar to normal rats without defect. All these results indicate that apt-CaF$_2$@BGs can be used as an efficient tool for monitoring of osteoblast expression, holding great promise for the investigation of biomineralization mechanisms.

CONCLUSION

In this work, the excellent performance of bioactive CaF_2-matrixed integrated nanodepots in biomineralization promotion and monitoring was presented. Such nanodepots can not only accelerate the growth of mineral crystals but also enhance the expression of organic fibrillar collagens, synergistically improving the progress of biomineralization. Besides, the integrated nanodepots display excellent ability in improving *in vivo* biomineralization and further promoting new bone regeneration. During the process of bone biomineralization, apt-nanodepots can be utilized to specifically recognize osteoblasts for biomineralization monitoring. The multifunctional nanodepots offer a vivid example for the regulation and monitoring of biomineralization-related biological activities, holding great promise in applications of regenerative biomedicine and tissue engineering, such as diagnosis and treatment of bone-related diseases.

EXPERIMENTAL SECTION

Materials. Ytterbium oxide (Yb_2O_3, 99.99%), erbium oxide (Er_2O_3, 99.99%), oleic acid (OA), 1-octadecene (ODE), and bovine serum albumin (BSA) were purchased from Aladdin. Ethanol, methanol, cyclohexane, tetraethyl orthosilicate (TEOS), triethyl phosphates (TEP), sodium hydroxide (NaOH), sodium chloride (NaCl), ammonium fluoride (NH_4F), calcium nitrate tetrahydrate ($Ca(NO_3)_2 \cdot 4H_2O$), hydrochloric acid (HCl), ammonium hydroxide, glacial acetic acid, aminopropyltriethoxysilane (APTES), and hexadecyltrimethylammonium bromide (CTAB) were of analytical grade and purchased from Sinopharm Chemical Reagent Co. (China). 1-(3-(Dimethylamino)propyl)-3-ethylcarbodiimide (EDC), *N*-hydroxysuccinimide (NHS), and sulfosuccinimidyl-4-(*N*-maleimidomethyl)cyclohexane-1-carboxylate (Sulfo-SMCC) were purchased from Sigma-Aldrich. For the preparation of rare earth acetates $RE(CH_3COO)_3 \cdot 4H_2O$, corresponding earth oxides were dissolved in acetic acid at 140 °C, and then the solvents were evaporated to obtain the final products. Improved SBF was prepared by adding 8 μL of 5% (w/v) sodium azide (NaN_3) into 10 mL of commercial SBF. The addition of NaN_3 aims to protect the collagen fiber from bacterial degradation. Preosteoblast MC3T3-E1 cells (catalog no. CL-0251) were purchased from Procell Life Science & Technology Co. (Wuhan, China). Osteoblasts were isolated from the bone marrow of mice. More detailed information on reagents used in cell-related experiments is included in the Supporting Information.

Nucleotide Sequences. All the nucleotides were purchased from NingBo Karebay Biochem Co., Ltd. The sequence of the osteoblast aptamer is 5′-SH-(A)$_9$-AGT CTG TTG GAC CGA ATC CCG TGG ACG CAC CCT TTG GAC G-3′. The sequence of the FITC-labeled aptamer is 5′-SH-(A)$_9$-AGT CTG TTG GAC CGA ATC CCG TGG ACG CAC CCT TTG GAC G-FITC-3′. The sequence of random DNA is 5′-(A)$_9$-SH-GAG AAC CTG AGT CAG TAT TGC GGA GAT TAG CCT AAT TGA C-3′.

Instrumentation. TEM characterizations were performed with a working voltage of 200 kV (JEOL, JEM-2100, Japan). The SEM images were obtained by a field-emission scanning electron microscopy (Zeiss Merlin Compact). Zeta potential measurements were performed using a Malvern Zeta Sizer Nano ZS system. The phases of nanoparticles were characterized using a D8 Advance X-ray diffractometer (Bruker) with Cu Kα radiation (λ = 1.5406 Å). Luminescent spectra were obtained using a Hitachi F-4600 fluorescence spectrometer equipped with a 980 nm laser. The ultraviolet−visible (UV−vis) absorption spectrum was collected on a UV-2550 scanning spectrophotometer (Shimadzu). Cell imaging was performed on a confocal laser scanning microscope (FV1200, Olympus, Japan) with a 980 nm laser excitation. Flow cytometry measurements were collected on a FACS AriaIII/BD cytometer. The imaging experiments for distribution of apt-nanodepots in the main organs and bone were carried out on an IVIS Lumina XR imaging

system (Caliper, America). Microcomputed tomography reconstruction was carried out by the μ-CT imaging system (μ-CT50, Bruker Skyscan1172, Germany). The histomorphological analysis was recorded by an Olympus DP72 microscope (Olympus, Japan).

Synthesis of CaF_2 Nanoparticles. The CaF_2 nanoparticles were synthesized according to a reported method with minor modification.[36] Specifically, 1 mmol of $Ca(CH_3COO)_2 \cdot H_2O$ was added into a three-necked flask containing 5 mL of OA and 15 mL of ODE. Next, under the protection of Ar flow, the mixture was heated to 160 °C with stirring and kept for 30 min. After cooling to 50 °C, 0.0925 g of NH_4F and 0.1000 g of NaOH were dissolved into 10 mL of methanol, and the solution was injected into the flask. Subsequently, the mixture was heated to 110 °C for 30 min to remove methanol and then heated to 280 °C under Ar protection for 60 min. The obtained products were precipitated and washed with 20 mL of ethanol, finally dispersed in 10 mL of cyclohexane. For the synthesis of CaF_2:Yb,Er upconversion nanoparticles, 0.1436 g of $Ca(CH_3COO)_2 \cdot H_2O$, 0.076 g of $Yb(CH_3COO)_3 \cdot 4H_2O$, and 0.0021 g of $Er(CH_3COO)_3 \cdot 4H_2O$ were first added into the flask, and the subsequent procedure is the same as that of CaF_2 nanoparticles. To enhance the upconversion luminescence, the as-prepared CaF_2:Yb,Er core nanoparticles were then coated with CaF_2 shells. In brief, 0.1762 g of $Ca(CH_3COO)_2 \cdot H_2O$ was added into the three-necked flask containing 5 mL of OA and 15 mL of ODE and then heated to 160 °C for 30 min under Ar flow. After cooling to 50 °C, 1 mL of cyclohexane containing the CaF_2:Yb,Er core nanoparticles was injected into the flasks. Then, the mixture was heated to 110 °C for 30 min, and then 10 mL of methanol solution containing 0.0925 g of NH_4F and 0.1000 g of NaOH was injected into the flasks. After that, the mixture was heated to 110 °C for 30 min again and heated to 280 °C under Ar flow for 90 min. The produced core−shell nanoparticles were precipitated by the addition of ethanol, separated by centrifugation, and then washed with ethanol. Two shell-coated CaF_2 nanoparticles were obtained by repeating the shell-coating procedure.

Synthesis of BSA-Coated CaF_2 Nanoparticles (CaF_2@BSA). Functionalization of CaF_2 nanoparticles with BSA was implemented according to previous work.[39] In a typical experiment, 50 mg of BSA was dissolved into 20 mL of water. Then, 50 mg of CaF_2 nanoparticles was dispersed in 2 mL of chloroform, and then the BSA solution injected under ultrasound. The ultrasonic treatment was maintained for 10 min. Next, the mixture was evaporated to form a clear solution, separated by centrifugation, and washed with water three times.

Synthesis of CaF_2@BGs-Integrated Nanodepots. The synthesis of CaF_2@BGs nanodepots was according to the previously reported literature with minor modification.[40] In brief, 500 μL of Igepal CO-520 was dissolved into 10 mL of cyclohexane, and the 500 μL of CaF_2@BSA solution was added. The mixture was stirred for 3 h, followed by the addition of ammonium hydroxide (70 μL) and stirring for another 2 h. After that, 400 μL of $Ca(NO_3)_2 \cdot 4H_2O$ solution (0.076 g mL^{-1}) and 6 μL of TEP were successively added into the mixture with stirring for 30 min. Subsequently, 200 μL of TEOS was added into the mixture, and the reaction was maintained for 24 h. Finally, the obtained products were collected by centrifugation, washed with ethanol, and redispersed in ethanol for further use. CaF_2:Yb,Er@BGs nanodepots are synthesized with the same procedure.

Preparation of APTES-Functionalized CaF_2:Yb,Er@BGs (NH_2-CaF_2@BGs). The obtained CaF_2:Yb,Er@BGs nanodepots were dispersed in 18 mL of ethanol containing 50 μL of APTES. The mixture solution was then heated at 80 °C for 1 h. After cooled to room temperature, the products were collected by centrifugation and washed several times.

Preparation of Aptamer-Functionalized CaF_2:Yb,Er@BGs Nanodepots (apt-Nanodepots). Briefly, a mixture solution containing 1 mg of NH_2-nanodepots and 800 μL of HEPES buffer solution was added to 200 μL of DMSO containing 0.4 mg of Sulfo-SMCC. After incubation at 25 °C for 2 h, the activated nanodepots were centrifuged and washed three times with PBS. Then, the activated nanoparticles were dispersed in PBS (1 mL). After that, aptamer (2 nmol) was added to the mixture solution, and the above

solution was incubated at 25 °C for 12 h. Finally, the apt-nanodepots were collected and washed with water. The as-prepared apt-nanodepots was redispersed in PBS buffer solution (pH 7.4, 10 mM) and stored at 4 °C. Conjugation of rDNA with nanodepots was done according to a similar method.

Preparation of FITC-Labeled Aptamer-Functionalized Ca-F₂:Yb,Er@BGs Nanodepots (FITC-apt-Nanodepots). The method for preparation of FITC-apt-nanodepots is similar to that of apt-nanodepots. NH_2-nanodepots were first activated by Sulfo-SMCC and then conjugated with FITC-labeled aptamer to form FITC-apt-nanodepots.

Mineralization of Fibrillar Collagens Based on Nanodepots. Fibrillar collagens were first assembled onto the copper girds. In brief, 80 μL of 0.2 mg mL⁻¹ fibrillar collagen stock solution was dropped into a Petri dish, and then a 300-mesh carbon-and-Formvar gold TEM grid was placed into the drop. The solution was placed under a steam of ammonium hydroxide to neutralize it until the pH reached 8. Next, the grid was taken out, and then, 0.3 M EDC and 0.1 M NHS were used to cross-link the collagens for 4 h. For mineralization, 2 mL of 1 mg mL⁻¹ nanodepots was enclosed in a dialysis bag, and then the bag was immersed into 10 mL of improved SBF. Immediately, the TEM grid assembled with collagen fibers was placed into the solution for a certain time. Specifically, for the CaF_2@BGs-promoted mineralization, TEM grids were immersed into CaF_2@BGs-containing SBF for 24, 48, 96, and 144 h, respectively. For comparison, TEM girds were immersed into the systems containing CaF_2 and PBS for 48 h, respectively. After that, the TEM grid was stained with 2% phosphotungstic acid solution for 1 min and then characterized with TEM.

In Vitro Cytotoxity Assays. The preosteoblast MC3T3-E1 cells were cultured with different concentrations of CaF_2@BGs nanodepots (0, 5, 10, 25, 50, and 100 μg mL⁻¹) at 37 °C in α-MEM medium for 1, 3, and 5 days. Then, standard MTT assay, total DNA content, and total protein content measurements were further utilized to measure the viability of osteoblasts. More details of MTT are included in the Supporting Information. The total DNA content and total protein content were determined by using the mammalian genomic DNA extraction kit (Beyotime Biotechnology) and bicinchoninic acid protein assay kit (Sigma-Aldrich), respectively.

In Vitro Mineralization. In osteogenic-inducing medium (α-MEM containing 10% FBS, 50 μg mL⁻¹ ascorbic acid, 10 nM dexamethasone, and 10 mM β-glycerophosphate), 10^5 MC3T3-E1 cells were incubated with PBS, F-free nanodepots, or integrated nanodepots. It is noted that the concentrations of nanoparticles are kept at 100 μg mL⁻¹. Every 2 days, the osteogenic-inducing medium was replaced. All groups of cells were cultured at 37 °C in a 5% CO_2 incubator. After that, ALP staining and Alizarin Red S staining were performed to evaluate the mineralization degree of osteoblasts at day 7 and day 21, respectively (more details in the Supporting Information). For the confocal fluorescence imaging, tetracycline and DyLight-labeled antibody were used to label crystals and collagens, respectively. At culture day 10, tetracycline was added into the cultures with a concentration of 50 μg mL⁻¹. At day 12, the cultured osteoblasts were fixed with paraformaldehyde (PFA) solution and then subjected to the immunofluorescence procedure.

Targeted Imaging and Flow Cytometric Analysis of Osteoblasts. The apt-nandepots (100 μL, 1 mg mL⁻¹) were incubated with osteoblasts at 37 °C in binding buffer for 1 h. Then the cells were washed three times with washing buffer and subjected to confocal fluorescence microscopy analysis with 980 nm laser excitation. For the flow cytometric analysis, FITC-apt (20 μL, 10 μM) and FITC-apt-CaF_2@BGs (200 μL, 1 mg mL⁻¹) were incubated with osteoblasts at 37 °C in binding buffer for 1 h. The resultant cells were washed with washing buffer and were further evaluated using flow cytometry.

In Vivo Cytotoxicity Study. Healthy Sprague−Dawley (SD) rats were purchased from Hubei Provincal Academy of Preventive Medicine (Wuhan, China). A 3-mm-diameter bone defect in rats (∼220 g) was filled with 10 mg of F-free nanodepots and integrated nanodepots, respectively. Bone defect without treatment was utilized as the control group. Over 30 days, the weights of the rats were recorded every 5 days. At day 28, the blood of the rats was collected for blood biochemistry and hematology examinations. The rats were sacrificed, and histological analysis of several organs including the heart, kidney, spleen, lung, and liver fixed in 4% paraformaldehyde was carried out.

In Vivo Biomineralization. SD rats of 8 weeks old were utilized as the in vivo model of subchondral bone defect with a diameter of 3 mm. The rats with bone defects were divided into three groups ($n = 3$ per group). A 10 mg amount of F-free nanodepots and integrated nanodepots was filled near the defect area of the rats, respectively. Then, all the rats were raised for 28 days. After that, all the rats were sacrificed and tibias were collected and fixed in 4% paraformaldehyde for 24 h at 4 °C. The biomineralization degree in vivo was evaluated by the μ-CT construction and H&E staining.

Preparation of Histological Tissue Samples. After micro-CT characterizations, the tibia samples were treated with 10% EDTA solution. The solution was refreshed twice a week, and the reaction system was shaken at room temperature. After 12 weeks, the samples were treated with gradient dehydration and embedded in paraffin for subsequent sections. Then, the sections were collected and fixed onto a polylysine-coated slide for further H&E staining.

In Vivo Bioimaging Based apt-Nanodepots. Typically, apt-nanodepots (0.2 mL, 5 mg) were intravenously injected into healthy SD rats for biodistribution study. Then, the rats were sacrificed at 2, 4, 8, 12, and 24 h, respectively. The main organs including the heart, kidney, spleen, lung, liver, and tibias were collected for imaging with 980 nm excitation. For monitoring of the biomineralization process in vivo, the SD rat models of subchondral bone defects were treated with integrated nanodepots. After the rats were raised for 1 week, 2 weeks, 3 weeks, and 4 weeks, apt-nanodepots (0.2 mL, 5 mg) were intravenously injected into the rats and tibias were collected at 8 h after injection. For visualization of the repair performance of different groups, apt-nanodepots (0.2 mL, 5 mg) were intravenously injected into the SD rat model of bone defect treated with F-free nanodepots and integrated nanodepots and without treatment at day 28.

Statistical Data Treatment. The statistical data were calculated using GraphPad Prism 8 and Microsoft Excel 2010 software, then presented as mean ± standard deviation (SD). All the P values were calculated by unpaired two-tailed Student's t-test, and the 0.05 level of significance ($P < 0.05$) was adopted throughout this work. The statistical significance provided is meant to be compared with the group treated with integrated nanodepots. The two P values in each figure are calculated between the control group and the group treated with integrated nanodepots, and between the group treated with F-free nanodepots and treated with integrated nanodepots, respectively.

All surgical procedures were approved by the Ethics Committee for Animal Research, Wuhan University, China.

ASSOCIATED CONTENT

ⓈI Supporting Information

The Supporting Information is available free of charge at https://pubs.acs.org/doi/10.1021/acsnano.0c08013.

> More details of materials and methods; TEM images, XRD patterns, and upconversion luminescent spectra of the CaF_2 nanoparticles and CaF_2@BGs nanocomposites; ALP staining images and corresponding quantitative analysis; confocal microscopy images of osteoblasts treated with apt-nanodepots for different times; body-weight changes of rats; histological analysis of major organs; blood biochemistry and hematology examination (PDF)

AUTHOR INFORMATION

Corresponding Authors

Quan Yuan − Key Laboratory of Analytical Chemistry for Biological Medicine (Ministry of Education), College of

Chemistry and Molecular Sciences, Wuhan University, Wuhan 430072, China; Institute of Chemical Biology and Nanomedicine, State Key Laboratory of Chemo/Biosensing and Chemometrics, College of Chemistry and Chemical Engineering, Hunan University, Changsha 410082, China; ⊙ orcid.org/0000-0002-3085-431X; Email: yuanquan@whu.edu.cn

Yufeng Zhang − State Key Laboratory Breeding Base of Basic Science of Stomatology (Hubei-MOST) and Key Laboratory of Oral Biomedicine (Ministry of Education), School and Hospital of Stomatology, Wuhan University, Wuhan 430072, China; ⊙ orcid.org/0000-0001-8702-5291; Email: zyf@whu.edu.cn

Authors

Zhihao Li − Key Laboratory of Analytical Chemistry for Biological Medicine (Ministry of Education), College of Chemistry and Molecular Sciences, Wuhan University, Wuhan 430072, China

Haoran Liu − Key Laboratory of Analytical Chemistry for Biological Medicine (Ministry of Education), College of Chemistry and Molecular Sciences, Wuhan University, Wuhan 430072, China

Rui Wang − State Key Laboratory Breeding Base of Basic Science of Stomatology (Hubei-MOST) and Key Laboratory of Oral Biomedicine (Ministry of Education), School and Hospital of Stomatology, Wuhan University, Wuhan 430072, China

Chenhui Ji − Institute of Chemical Biology and Nanomedicine, State Key Laboratory of Chemo/Biosensing and Chemometrics, College of Chemistry and Chemical Engineering, Hunan University, Changsha 410082, China

Yan Wei − State Key Laboratory Breeding Base of Basic Science of Stomatology (Hubei-MOST) and Key Laboratory of Oral Biomedicine (Ministry of Education), School and Hospital of Stomatology, Wuhan University, Wuhan 430072, China

Miusi Shi − State Key Laboratory Breeding Base of Basic Science of Stomatology (Hubei-MOST) and Key Laboratory of Oral Biomedicine (Ministry of Education), School and Hospital of Stomatology, Wuhan University, Wuhan 430072, China; ⊙ orcid.org/0000-0001-8679-4013

Yingqian Wang − Key Laboratory of Analytical Chemistry for Biological Medicine (Ministry of Education), College of Chemistry and Molecular Sciences, Wuhan University, Wuhan 430072, China

Yaping Du − School of Materials Science and Engineering & National Institute for Advanced Materials, Key Laboratory of Advanced Energy Materials Chemistry, Tianjin Key Lab for Rare Earth Materials and Applications, Centre for Rare Earth and Inorganic Functional Materials, Nankai University, Tianjin 300350, China

Chunhua Yan − School of Materials Science and Engineering & National Institute for Advanced Materials, Key Laboratory of Advanced Energy Materials Chemistry, Tianjin Key Lab for Rare Earth Materials and Applications, Centre for Rare Earth and Inorganic Functional Materials, Nankai University, Tianjin 300350, China; ⊙ orcid.org/0000-0002-0581-2951

Complete contact information is available at:
https://pubs.acs.org/10.1021/acsnano.0c08013

Author Contributions

§Z. Li, H. Liu, and R. Wang contributed equally to this work.

Notes

The authors declare no competing financial interest.

REFERENCES

(1) Thompson, K. H.; Orvig, C. Boon and Bane of Metal Ions in Medicine. Science 2003, 300, 936−939.

(2) Palm, W.; Thompson, C. B. Nutrient Acquisition Strategies of Mammalian Cells. Nature 2017, 546, 234−242.

(3) Muller, W. E. G.; Schroder, H. C.; Wang, X. Inorganic Polyphosphates as Storage for and Generator of Metabolic Energy in the Extracellular Matrix. Chem. Rev. 2019, 119, 12337−12374.

(4) Pereto, J. Out of Fuzzy Chemistry: From Prebiotic Chemistry to Metabolic Networks. Chem. Soc. Rev. 2012, 41, 5394−5403.

(5) Yu, N.; Huang, L.; Zhou, Y.; Xue, T.; Chen, Z.; Han, G. Near-Infrared-Light Activatable Nanoparticles for Deep-Tissue-Penetrating Wireless Optogenetics. Adv. Healthcare Mater. 2019, 8, 1801132.

(6) Riccardi, L.; Genna, V.; De Vivo, M. Metal-Ligand Interactions in Drug Design. Nat. Rev. Chem. 2018, 2, 100−112.

(7) Mirts, E. N.; Damodaran, A. B.; Lu, Y. Understanding and Modulating Metalloenzymes with Unnatural Amino Acids, Non-Native Metal Ions, and Non-Native Metallocofactors. Acc. Chem. Res. 2019, 52, 935−944.

(8) Chen, S.; Weitemier, A. Z.; Zeng, X.; He, L.; Wang, X.; Tao, Y.; Huang, A. J. Y.; Hashimotodani, Y.; Kano, M.; Iwasaki, H.; Parajuli, L. K.; Okabe, S.; Teh, D. B. L.; All, A. H.; Kimura, I. T.; Tanaka, K. F.; Liu, X.; McHugh, T. J. Near-Infrared Deep Brain Stimulation via Upconversion Nanoparticle-Mediated Optogenetics. Science 2018, 359, 679−684.

(9) Dudev, T.; Lim, C. Competition among Metal Ions for Protein Binding Sites: Determinants of Metal Ion Selectivity in Proteins. Chem. Rev. 2014, 114, 538−556.

(10) Lin, Y.; Yang, Z.; Lake, R. J.; Zheng, C.; Lu, Y. Enzyme-Mediated Endogenous and Bioorthogonal Control of a DNAzyme Fluorescent Sensor for Imaging Metal Ions in Living Cells. Angew. Chem., Int. Ed. 2019, 58, 17061−17067.

(11) Weichold, V.; Milbredt, D.; Van Pee, K. H. Specific Enzymatic Halogenation—From the Discovery of Halogenated Enzymes to Their Applications in Vitro and in Vivo. Angew. Chem., Int. Ed. 2016, 55, 6374−6389.

(12) Ai, X.; Lyu, L.; Zhang, Y.; Tang, Y.; Mu, J.; Liu, F.; Zhou, Y.; Zuo, Z.; Liu, G.; Xing, B. Remote Regulation of Membrane Channel Activity by Site-Specific Localization of Lanthanide-Doped Upconversion Nanocrystals. Angew. Chem., Int. Ed. 2017, 56, 3031−3035.

(13) Pols, T.; Sikkema, H. R.; Gaastra, B. F.; Frallicciardi, J.; Smigiel, W. M.; Singh, S.; Poolman, B. A Synthetic Metabolic Network for Physicochemical Homeostasis. Nat. Commun. 2019, 10, 4239.

(14) Shao, C.; Zhao, R.; Jiang, S.; Yao, S.; Wu, Z.; Jin, B.; Yang, Y.; Pan, H.; Tang, R. Citrate Improves Collagen Mineralization via Interface Wetting: A Physicochemical Understanding of Biomineralization Control. Adv. Mater. 2018, 30, 1704876.

(15) Smeets, P. J.; Cho, K. R.; Kempen, R. G.; Sommerdijk, N. A.; De Yoreo, J. J. Calcium Carbonate Nucleation Driven by Ion Binding in a Biomimetic Matrix Revealed by in Situ Electron Microscopy. Nat. Mater. 2015, 14, 394−399.

(16) Liu, C.; Zhai, H.; Zhang, Z.; Li, Y.; Xu, X.; Tang, R. Cells Recognize and Prefer Bone-Like Hydroxyapatite: Biochemical Understanding of Ultrathin Mineral Platelets in Bone. ACS Appl. Mater. Interfaces 2016, 8, 29997−30004.

(17) Reznikov, N.; Steele, J. A. M.; Fratzl, P.; Stevens, M. M. A Materials Science Vision of Extracellular Matrix Mineralization. Nat. Rev. Mater. 2016, 1, 16041.

(18) de Melo Pereira, D.; Habibovic, P. Biomineralization-Inspired Material Design for Bone Regeneration. Adv. Healthcare Mater. 2018, 7, 1800700.

(19) Yao, S.; Jin, B.; Liu, Z.; Shao, C.; Zhao, R.; Wang, X.; Tang, R. Biomineralization: From Material Tactics to Biological Strategy. *Adv. Mater.* **2017**, *29*, 1605903.

(20) Chang, H. H.; Chien, M. J.; Kao, C. C.; Chao, Y. J.; Yu, P. T.; Chang, C. Y.; Huang, S. J.; Lee, Y. L.; Chan, J. C. Structural Characterization of Fluoride Species in Shark Teeth. *Chem. Commun.* **2017**, *53*, 3838−3841.

(21) Wang, Y.; Hu, X.; Zhang, L.; Zhu, C.; Wang, J.; Li, Y.; Wang, Y.; Wang, C.; Zhang, Y.; Yuan, Q. Bioinspired Extracellular Vesicles Embedded with Black Phosphorus for Molecular Recognition-Guided Biomineralization. *Nat. Commun.* **2019**, *10*, 2829.

(22) Fukao, K.; Nonoyama, T.; Kiyama, R.; Furusawa, K.; Kurokawa, T.; Nakajima, T.; Gong, J. P. Anisotropic Growth of Hydroxyapatite in Stretched Double Network Hydrogel. *ACS Nano* **2017**, *11*, 12103−12110.

(23) Hu, X.; Wang, Y.; Tan, Y.; Wang, J.; Liu, H.; Wang, Y.; Yang, S.; Shi, M.; Zhao, S.; Zhang, Y.; Yuan, Q. A Difunctional Regeneration Scaffold for Knee Repair Based on Aptamer-Directed Cell Recruitment. *Adv. Mater.* **2017**, *29*, 1605235.

(24) Liang, C.; Guo, B.; Wu, H.; Shao, N.; Li, D.; Liu, J.; Dang, L.; Wang, C.; Li, H.; Li, S.; Lau, W. K.; Cao, Y.; Yang, Z.; Lu, C.; He, X.; Au, D. W.; Pan, X.; Zhang, B. T.; Lu, C.; Zhang, H.; et al. Aptamer-Functionalized Lipid Nanoparticles Targeting Osteoblasts as a Novel RNA Interference-Based Bone Anabolic Strategy. *Nat. Med.* **2015**, *21*, 288−294.

(25) Sun, Y.; Ye, X.; Cai, M.; Liu, X.; Xiao, J.; Zhang, C.; Wang, Y.; Yang, L.; Liu, J.; Li, S.; Kang, C.; Zhang, B.; Zhang, Q.; Wang, Z.; Hong, A.; Wang, X. Osteoblast-Targeting-Peptide Modified Nanoparticle for siRNA/microRNA Delivery. *ACS Nano* **2016**, *10*, 5759−5768.

(26) Wang, Y.; Wang, J.; Hao, H.; Cai, M.; Wang, S.; Ma, J.; Li, Y.; Mao, C.; Zhang, S. *In Vitro* and *in Vivo* Mechanism of Bone Tumor Inhibition by Selenium-Doped Bone Mineral Nanoparticles. *ACS Nano* **2016**, *10*, 9927−9937.

(27) Wang, Z.; Ouyang, Y.; Wu, Z.; Zhang, L.; Shao, C.; Fan, J.; Zhang, L.; Shi, Y.; Zhou, Z.; Pan, H.; Tang, R.; Fu, B. A Novel Fluorescent Adhesive-Assisted Biomimetic Mineralization. *Nanoscale* **2018**, *10*, 18980−18987.

(28) Luo, Y. J.; Takeuchi, T.; Koyanagi, R.; Yamada, L.; Kanda, M.; Khalturina, M.; Fujie, M.; Yamasaki, S. I.; Endo, K.; Satoh, N. The *Lingula* Genome Provides Insights into Brachiopod Evolution and the Origin of Phosphate Biomineralization. *Nat. Commun.* **2015**, *6*, 8301.

(29) Boonrungsiman, S.; Gentleman, E.; Carzaniga, R.; Evans, N. D.; McComb, D. W.; Porter, A. E.; Stevens, M. M. The Role of Intracellular Calcium Phosphate in Osteoblast-Mediated Bone Apatite Formation. *Proc. Natl. Acad. Sci. U. S. A.* **2012**, *109*, 14170−14175.

(30) Yang, L.; Perez-Amodio, S.; Barrere-De Groot, F. Y.; Everts, V.; van Blitterswijk, C. A.; Habibovic, P. The Effects of Inorganic Additives to Calcium Phosphate on *in Vitro* Behavior of Osteoblasts and Osteoclasts. *Biomaterials* **2010**, *31*, 2976−2989.

(31) Busch, S.; Schwarz, U.; Kniep, R. Morphogenesis and Structure of Human Teeth in Relation to Biomimetically Grown Fluorapatite-Gelatine Composites. *Chem. Mater.* **2001**, *13*, 3260−3271.

(32) Veernala, I.; Giri, J.; Pradhan, A.; Polley, P.; Singh, R.; Yadava, S. K. Effect of Fluoride Doping in Laponite Nanoplatelets on Osteogenic Differentiation of Human Dental Follicle Stem Cells (hDFSCs). *Sci. Rep.* **2019**, *9*, 915.

(33) Jones, J. R. Review of Bioactive Glass: From Hench to Hybrids. *Acta Biomater.* **2013**, *9*, 4457−4486.

(34) Brauer, D. S. Bioactive Glasses—Structure and Properties. *Angew. Chem., Int. Ed.* **2015**, *54*, 4160−4181.

(35) Dong, N. N.; Pedroni, M.; Piccinelli, F.; Conti, G.; Sbarbati, A.; Hernandez, J. E. R.; Maestro, L. M.; Cruz, M. C. I.; Rodriguez, F. S.; Juarranz, A.; Chen, F.; Vetrone, F.; Capobianco, J. A.; Sole, J. G.; Bettinelli, M.; Jaque, D.; Speghini, A. NIR-to-NIR Two-Photon Excited CaF_2:Tm^{3+},Yb^{3+} Nanoparticles: Multifunctional Nanoprobes for Highly Penetrating Fluorescence Bio-Imaging. *ACS Nano* **2011**, *5*, 8665−8671.

(36) Zheng, W.; Zhou, S.; Chen, Z.; Hu, P.; Liu, Y.; Tu, D.; Zhu, H.; Li, R.; Huang, M.; Chen, X. Sub-10 nm Lanthanide-Doped CaF_2 Nanoprobes for Time-Resolved Luminescent Biodetection. *Angew. Chem., Int. Ed.* **2013**, *52*, 6671−6676.

(37) Li, Z.; Zhang, Y.; Huang, L.; Yang, Y.; Zhao, Y.; El-Banna, G.; Han, G. Nanoscale "Fluorescent Stone": Luminescent Calcium Fluoride Nanoparticles as Theranostic Platforms. *Theranostics* **2016**, *6*, 2380−2393.

(38) Liu, Y.; Tu, D.; Zhu, H.; Chen, X. Lanthanide-Doped Luminescent Nanoprobes: Controlled Synthesis, Optical Spectroscopy, and Bioapplications. *Chem. Soc. Rev.* **2013**, *42*, 6924−6958.

(39) Du, H.; Yu, J.; Guo, D.; Yang, W.; Wang, J.; Zhang, B. Improving the MR Imaging Sensitivity of Upconversion Nanoparticles by an Internal and External Incorporation of the Gd^{3+} Strategy for *in Vivo* Tumor-Targeted Imaging. *Langmuir* **2016**, *32*, 1155−1165.

(40) Fan, W.; Shen, B.; Bu, W.; Chen, F.; Zhao, K.; Zhang, S.; Zhou, L.; Peng, W.; Xiao, Q.; Xing, H.; Liu, J.; Ni, D.; He, Q.; Shi, J. Rattle-Structured Multifunctional Nanotheranostics for Synergetic Chemo-/Radiotherapy and Simultaneous Magnetic/Luminescent Dual-Mode Imaging. *J. Am. Chem. Soc.* **2013**, *135*, 6494−6503.

(41) Wang, Z.; Ma, G.; Liu, X. Y. Will Fluoride Toughen or Weaken Our Teeth? Understandings Based on Nucleation, Morphology, and Structural Assembly. *J. Phys. Chem. B* **2009**, *113*, 16393−16399.

(42) Kim, D.; Lee, B.; Thomopoulos, S.; Jun, Y. S. The Role of Confined Collagen Geometry in Decreasing Nucleation Energy Barriers to Intrafibrillar Mineralization. *Nat. Commun.* **2018**, *9*, 962.

(43) Hamm, L. M.; Giuffre, A. J.; Han, N.; Tao, J.; Wang, D.; De Yoreo, J. J.; Dove, P. M. Reconciling Disparate Views of Template-Directed Nucleation through Measurement of Calcite Nucleation Kinetics and Binding Energies. *Proc. Natl. Acad. Sci. U. S. A.* **2014**, *111*, 1304−1309.

(44) Rahman, M. S.; Akhtar, N.; Jamil, H. M.; Banik, R. S.; Asaduzzaman, S. M. TGF-β/BMP Signaling and Other Molecular Events: Regulation of Osteoblastogenesis and Bone Formation. *Bone Res.* **2015**, *3*, 15005.

(45) Han, Y.; You, X.; Xing, W.; Zhang, Z.; Zou, W. Paracrine and Endocrine Actions of Bone—The Functions of Secretory Proteins from Osteoblasts, Osteocytes, and Osteoclasts. *Bone Res.* **2018**, *6*, 16.

(46) Dirckx, N.; Moorer, M. C.; Clemens, T. L.; Riddle, R. C. The Role of Osteoblasts in Energy Homeostasis. *Nat. Rev. Endocrinol.* **2019**, *15*, 651−665.

(47) Rauch, A.; Haakonsson, A. K.; Madsen, J. G. S.; Larsen, M.; Forss, I.; Madsen, M. R.; Van Hauwaert, E. L.; Wiwie, C.; Jespersen, N. Z.; Tencerova, M.; Nielsen, R.; Larsen, B. D.; Rottger, R.; Baumbach, J.; Scheele, C.; Kassem, M.; Mandrup, S. Osteogenesis Depends on Commissioning of a Network of Stem Cell Transcription Factors That Act as Repressors of Adipogenesis. *Nat. Genet.* **2019**, *51*, 716−727.

(48) Tsoi, K. M.; MacParland, S. A.; Ma, X. Z.; Spetzler, V. N.; Echeverri, J.; Ouyang, B.; Fadel, S. M.; Sykes, E. A.; Goldaracena, N.; Kaths, J. M.; Conneely, J. B.; Alman, B. A.; Selzner, M.; Ostrowski, M. A.; Adeyi, O. A.; Zilman, A.; McGilvray, I. D.; Chan, W. C. W. Mechanism of Hard-Nanomaterial Clearance by the Liver. *Nat. Mater.* **2016**, *15*, 1212−1221.

(49) Hu, K.; Olsen, B. R. Osteoblast-Derived VEGF Regulates Osteoblast Differentiation and Bone Formation during Bone Repair. *J. Clin. Invest.* **2016**, *126*, 509−526.

(50) Dimitriou, R.; TsiridisM, E.; Giannoudis, P. V. Current Concepts of Molecular Aspects of Bone Healing. *Injury* **2005**, *36*, 1392−1404.